HHS Public Access

Author manuscript

Neuroimage. Author manuscript; available in PMC 2017 May 15.

Published in final edited form as:

Neuroimage. 2016 May 15; 132: 104–114. doi:10.1016/j.neuroimage.2016.02.004.

In vivo quantification of demyelination and recovery using compartment-specific diffusion MRI metrics validated by electron microscopy

Ileana O. Jelescu[*], **Magdalena Zurek**, **Kerryanne V. Winters**, **Jelle Veraart**, **Anjali Rajaratnam**, **Nathanael S. Kim**, **James S. Babb**, **Timothy M. Shepherd**, **Dmitry S. Novikov**, **Sungheon G. Kim**, and **Els Fieremans**

Center for Biomedical Imaging, Department of Radiology, New York University School of Medicine, New York, NY, USA

Abstract

There is a need for accurate quantitative non-invasive biomarkers to monitor myelin pathology *in vivo* and distinguish myelin changes from other pathological features including inflammation and axonal loss. Conventional MRI metrics such as T_2, magnetization transfer ratio and radial diffusivity have proven sensitivity but not specificity. In highly coherent white matter bundles, compartment-specific white matter tract integrity (WMTI) metrics can be directly derived from the diffusion and kurtosis tensors: axonal water fraction, intra-axonal diffusivity, and extra-axonal radial and axial diffusivities. We evaluate the potential of WMTI to quantify demyelination by monitoring the effects of both acute (6 weeks) and chronic (12 weeks) cuprizone intoxication and subsequent recovery in the mouse corpus callosum, and compare its performance with that of conventional metrics (T_2, magnetization transfer, and DTI parameters). The changes observed *in vivo* correlated with those obtained from quantitative electron microscopy image analysis. A 6-week intoxication produced a significant decrease in axonal water fraction ($p < 0.001$), with only mild changes in extra-axonal radial diffusivity, consistent with patchy demyelination, while a 12-week intoxication caused a more marked decrease in extra-axonal radial diffusivity ($p = 0.0135$), consistent with more severe demyelination and clearance of the extra-axonal space. Results thus revealed increased specificity of the axonal water fraction and extra-axonal radial diffusivity parameters to different degrees and patterns of demyelination. The specificities of these parameters were corroborated by their respective correlations with microstructural features: the axonal water fraction correlated significantly with the electron microscopy derived total axonal water fraction ($\rho = 0.66$; $p = 0.0014$) but not with the g-ratio, while the extra-axonal radial diffusivity correlated with the g-ratio ($\rho = 0.48$; $p = 0.0342$) but not with the electron microscopy derived axonal water fraction. These parameters represent promising candidates as clinically feasible biomarkers of demyelination and remyelination in the white matter.

[*]Corresponding author: Address all correspondence to: Ileana Jelescu, Department of Radiology, NYU Langone Medical Center, 660 First Avenue, 2nd floor, New York, NY 10016. ijelescu@gmail.com, Tel.: (212) 263-4808; Fax: (212) 263-4830.

Keywords

white matter tract integrity; demyelination; cuprizone; diffusion MRI; biomarker

1. Introduction

Demyelination and/or remyelination are important components of several complex pathologies, such as multiple sclerosis (Grossman and McGowan, 1998; Hommes, 1980), as well as Alzheimer's disease (Brun and Englund, 1986), schizophrenia (Davis et al., 2003) and traumatic brain injury (Kinnunen et al., 2011). Non-invasive specific monitoring of demyelination and remyelination could provide clinically-important information on disease progression and treatment efficacy. Although the development of such biomarkers has come a long way (Galvin et al., 1976), it is still a vast area of research (Filippi et al., 2014; Tomioka and Matsui, 2014).

Studies of cuprizone intoxication and recovery in mice have proven highly insightful for evaluating the sensitivity and specificity of biomarker candidates to myelin changes. Indeed, cuprizone intoxication is characterized by highly reproducible dynamics and patterns in the mouse brain, and its molecular and cellular neuropathology have been studied extensively (Praet et al., 2014). Cuprizone intoxication leads to the death of oligodendrocytes and subsequent demyelination, predominantly in the corpus callosum and superior cerebral peduncles (Skripuletz et al., 2011). The timecourse is characterized by complete demyelination in the corpus callosum after five weeks of cuprizone feeding. In the case of continued cuprizone diet, spontaneous remyelination occurs nonetheless in ∼50% axons at six weeks (Matsushima and Morell, 2001). Persistent cuprizone feeding causes a second complete demyelination by 10 weeks and some remyelination at 12 weeks. From the cessation of either acute (6 weeks) or chronic (12 weeks) intoxication, nearly complete remyelination occurs in the corpus callosum within six weeks (Matsushima and Morell, 2001; Skripuletz et al., 2008). The death of mature oligodendrocytes is accompanied by a strong inflammatory response. Microgliosis and astrogliosis build up at three weeks of intoxication and peak at 4.5 – 5 weeks; microglia then rapidly decline while astrocytes remain at a relatively elevated level for several weeks (Matsushima and Morell, 2001; Praet et al., 2014). A major advantage of cuprizone mouse studies is the possibility to directly correlate potential *in vivo* MR biomarker candidates for myelin, such as transverse relaxation time T_2, magnetization transfer ratio (MTR) or radial diffusivity (RD) from diffusion tensor imaging (DTI), against histology, immunohistochemistry or electron microscopy (EM). Here, we propose to evaluate the potential for White Matter Tract Integrity (WMTI) metrics derived from diffusion kurtosis imaging (DKI) as biomarkers for demyelination and remyelination, using the cuprizone mouse model.

DKI is an extension of DTI that quantifies the deviation from Gaussian diffusion in the tissues, thus also providing information on tissue complexity and/or heterogeneity (Jensen et al., 2005). Building on this method, the WMTI model was proposed to characterize the intra-and extra-axonal compartments in highly coherent white matter bundles, in terms of microstructural parameters directly derived from the diffusion and kurtosis tensors

(Fieremans et al., 2011; Fieremans et al., 2010). In WMTI, the intra-axonal space is modeled as a collection of sticks (cylinders with effective zero radius) and the extra-axonal space as a Gaussian anisotropic medium. Exchange between the intra- and extra-axonal spaces is neglected. The water MR signal originates from the collective intra-axonal space and the extra-axonal space. Water inside the myelin is not detected with the typical clinical diffusion MRI parameters. From this perspective, it should be noted that the compartment fractions correspond to "measurable water" fractions (possibly further weighted by different compartment T_2 values), and not to voxel volume fractions. This distinction is important since myelin takes up a non-negligible volume of a white matter voxel (up to 40% in adult corpus callosum (Lamantia and Rakic, 1990)). WMTI thus provides an estimate of the axonal water fraction (AWF), axonal diffusivity (D_a), and extra-axonal parallel and radial diffusivities ($D_{e,\parallel}$ and $D_{e,\perp}$) (Figures 1A and 1B). The model rests on two main assumptions: (i) highly aligned WM tracts (here we focus on the corpus callosum); (ii) the inherent duality of solutions for the parameter estimation problem (Jelescu et al., 2016) is resolved assuming $D_a \leq D_{e,\parallel}$ (rather than $D_a \geq D_{e,\parallel}$). The assumption (ii) affects mainly the values D_a and $D_{e,\parallel}$; the AWF and $D_{e,\perp}$ values are insensitive to this choice, and we are focussing on the latter metrics here. The extraction of WMTI metrics relies on DKI data which can be acquired in a clinically feasible time (< 10 min) (Grossman et al., 2015).

WMTI metrics are potentially more informative than empirical DTI because of their specificity to the underlying mesoscopic tissue architecture and disease mechanisms. It has been suggested that $D_{e,\perp}$ could be particularly sensitive to uniform demyelination and change in *g*-ratio, while AWF could be more sensitive to axonal loss and/or patchy demyelination (Novikov and Fieremans, 2012). Indeed, a decrease in AWF does not necessarily imply axonal loss but can also be an indirect effect of an increase in the extra-axonal volume fraction following demyelination, as illustrated in Figure 1C. Simultaneous decreases in $D_{e,\perp}$ and $D_{e,\parallel}$ could be attributed to extra-axonal crowding associated with inflammation, astrocytosis, gliosis etc, while decreases in D_a are indicative of acute intra-axonal injury (Grossman et al., 2015; Hui et al., 2012). Based on these features, WMTI has so far provided an insightful characterization of white matter changes in multiple sclerosis (Fieremans et al., 2012), Alzheimer's disease (Benitez et al., 2013; Fieremans et al., 2013), autism (Lazar et al., 2014), brain development (Jelescu et al., 2015), and traumatic brain injury (Grossman et al., 2015). WMTI metrics have also been shown to be sensitive to cuprizone induced demyelination and to correlate significantly with Solochrome myelin staining and microglia staining (Falangola et al., 2014).

In this work, we assess the potential for the WMTI metrics, and in particular for AWF and $D_{e,\perp}$, to track both demyelination and remyelination in the caudal corpus callosum (splenium) of cuprizone-fed mice, and compare it with that of conventional MR measures for myelin (T_2, MTR and RD). Additionally, we aim to validate the sensitivity and specificity of WMTI metrics to microstructural features determined using EM: myelin volume fraction, myelinated axonal water fraction, total axonal water fraction and *g*-ratio.

2. Materials and methods

2.1. Animals

All mice were treated in strict accordance with the National Institutes of Health Guide for the Care and Use of Laboratory Animals, and the experimental procedures were performed in accordance with the Institutional Animal Care and Use Committee at the New York University School of Medicine. We conducted an 18-week longitudinal study on 36 female C57BL/6 mice (Taconic Biosciences, Hudson, NY), all 8 weeks old at baseline. They were separated into three diet groups of 12 animals: the control ("Ctl") group received standard chow; the "Cpz6" and "Cpz12" groups received cuprizone-supplemented chow (0.2%, Sigma Aldrich, St. Louis, MO) for 6 and 12 weeks, respectively, followed by 6 weeks of recovery on standard chow (Figure 2A). *In vivo* MR imaging was performed at baseline, 6, 12 and 18 weeks. Subsets of animals from each diet group were sacrificed at 6, 12 and 18 weeks, following MR imaging, for histopathological evaluation using transmission EM.

2.2. MR Imaging

In vivo MRI was performed on a 7-T Biospec micro-MRI system (Bruker Biospin MRI, Ettlingen, Germany) equipped with a Bruker BGA-9S 750 mT/m gradient coil. Mice were anesthetized with 3% isoflurane in air and placed into a home-built quadrature volume coil. During imaging, anesthesia was maintained using 1% isoflurane in air delivered via a nose cone at a rate of 300 mL/min. The respiration rate (~60 breaths/min) and body temperature (maintained at 37°C) were monitored throughout the MR experiments (SA Instruments, Stony Brook, NY).

Diffusion MRI data was acquired along with T_2 and MTR. One 0.8-mm thick mid-sagittal slice was imaged with 112-μm in-plane resolution (matrix size: 256×160). Diffusion-weighted images were acquired using a 2D GRASE (Gradient and Spin Echo) sequence (Aggarwal et al., 2010; Oshio and Feinberg, 1991), with b-values of 1000 and 2000 s/mm^2 and 30 directions each, in addition to 6 $b = 0$ images (TR = 800 ms; TE = 49 ms; echo train length = 4; Δ = 16 ms; δ = 2 ms). T_2-weighted images were acquired using a multi-echo spin-echo sequence with eight echoes and echo-time increment = 7.1 ms (TR = 2 s; NA = 2). For MTR, two FLASH images (TR = 47 ms; TE = 5.5 ms; flip angle = 8°; NA = 40) were acquired with and without MT saturation pulse (Gaussian shape; frequency offset = 1.5 kHz; duration = 12 ms; peak power = 4.7 μT).

A single sagittal slice was chosen for two reasons. First, to maintain the total scan time within reasonable limits for mouse stability and survival. Second, the mid-sagittal slice is relatively easy to position consistently across multiple scans and mice; for correlations with EM, it was particularly important to reliably localize and extract blocks of tissue that had been part of the imaging slice, as well as to obtain blocks where the fibers were oriented normal to the cutting/imaging plane.

2.3. MR image processing

T_2 mapping: The amplitudes of echoes #2 through #8 (echo times = 14.2 ms – 56.8 ms) in each voxel were well characterized by a monoexponential decay, which was fit to generate

parametric T_2 maps. **MTR mapping**: The MT-on image was spatially registered to the MT-off image using FSL's FLIRT (Jenkinson et al., 2002; Jenkinson and Smith, 2001), and the MTR in each voxel was calculated as MTR = $(MT_{off} - MT_{on})/MT_{off} \times 100\%$. **Diffusion metrics**: Diffusion weighted images were co-registered to correct for motion, scan drift and eddy current distortions using Elastix (Klein et al., 2010). Following outlier removal, DKI analysis was performed using a constrained weighted linear least squares estimator (Collier et al., 2015; Veraart et al., 2013), followed by the derivation of the WMTI metrics (Fieremans et al., 2011), yielding maps of the DTI and DKI parameters – fractional anisotropy (FA), mean, axial and radial diffusivities (MD, AD, RD), mean, axial and radial kurtosis (MK, AK, RK), as well as of the WMTI parameters – axonal water fraction (AWF), axonal diffusivity (D_a), and extra-axonal parallel and radial diffusivities ($D_{e,\parallel}$ and $D_{e,\perp}$).

The splenium of the corpus callosum was chosen as the region of interest (ROI) because it is more readily affected by cuprizone than the genu or the body, and it remyelinates more rapidly upon cuprizone cessation (Steelman et al., 2012; Stidworthy et al., 2003). The splenium was segmented on the color-coded FA map (see Figure 3 for an example) using a semi-automated in-house tool in Matlab (The MathWorks, Natick, MA). Briefly, the red channel (medio-lateral orientation) of the color-coded FA map was extracted, and an area encompassing the corpus callosum was manually drawn and its contours refined using automated edge detection. The resulting ROI was divided into five equal segments, with the extremities corresponding to the splenium and genu, and the three central segments to the body. The splenium ROI mask was brought into T_2 and MTR spaces by registering the first $b = 0$ image from the diffusion-weighted series to the first T_2-weighted image from the multi-echo series, as well as to the MT-off image, and applying the transformations to the splenium mask (FSL FLIRT). The quality of the ROI registration between modalities was inspected visually. The linear registration was satisfactory since the GRASE sequence did not cause pronounced spatial distortions like EPI would.

The mean and standard deviation over the splenium were calculated for all MR metrics of interest, in each mouse and at each timepoint.

2.4. Electron microscopy

Animals were anesthetized using ketamine/xylazine (at 150 and 10 mg/kg, respectively) and perfused intracardially with 50 mL of phosphate-buffered saline mixed with heparin (5000 units/L), followed immediately by the fixative solution (2% formaldehyde, 2.5% glutaraldehyde, 0.1 M sucrose in 0.1 M phosphate-buffered saline). The brains were extracted and the splenium was excised. Two cone-shaped blocks of tissue were further fixed in the same fixative solution, followed by overnight 1% osmium tetroxide, then dehydrated in alcohol, acetone, and embedded in plastic. Nano-thick slices were cut in a microtome and imaged using a Phillips CM12 transmission electron microscope (Phillips, Andover, MA) equipped with a Gatan 4k × 2.7k digital camera (Gatan 785.CP17). Each electron micrograph covered an area of approximately 6×9 μm^2 at 2.36 nm spatial resolution.

Electron micrographs were analyzed using in-house developed macros in ImageJ[1]. Briefly, full myelin rings were automatically segmented based on image intensity thresholding, and myelinated axons were further detected by means of the connected-component analysis.

This processing yielded myelin volume fraction (MVF), myelinated axon volume fraction (mAVF) and myelinated axon count, which was normalized to the surface area of an EM image (mAxCount). The mAVF did not include the MVF; the "myelinated fiber volume fraction" therefore corresponds to mAVF + MVF. To account for unmyelinated axons, the total axonal volume fraction (tAVF) was estimated using CellProfiler (Lamprecht et al., 2007), while the total number of axons was counted manually and normalized to the surface area of an EM image (tAxCount). Finally, the *g*-ratio was derived as $\sqrt{\mathrm{tAVF}/(\mathrm{MVF}+\mathrm{tAVF})}$. Note that this is an "aggregate" *g*-ratio; it is the equivalent *g*-ratio if all the axons in an image had the same *g*-ratio. This processing was chosen in order to better account for unmyelinated and completely demyelinated axons (with a *g*-ratio of 1), for which a manual measurement of individual axon diameters would have considerably increased the processing effort. An example of the processing pipeline for the EM images is available as Supplementary Figure 1.

Because there is a conceptual difference between AVF and AWF (the former refers to a volume fraction, the latter is a fraction of "MR visible" water, which does not account for the myelin space), the EM-derived mAWF = mAVF/(1 – MVF) and tAWF = tAVF/(1 – MVF) were also calculated.

The EM image analysis was performed for three mice per timepoint and diet group, randomly chosen among the subgroup. Eight micrographs from each animal were analyzed, resulting in 423 myelinated and 1623 unmyelinated axons processed on average per animal. The mean and standard deviation were calculated for all EM measures in each animal.

2.5. Statistical analysis

For each MR measure, differences between diet groups at each timepoint were evaluated using ANCOVA (analysis of covariance) with Tukey-Kramer multiple comparison correction and mouse weight at baseline as covariate. Cohen's d was employed to assess the performance of each measure to discriminate between diet groups. Random coefficients regression (RCR) was used to estimate the linear rate of change in each outcome among animals in a given diet group while under cuprizone and to compare diet groups with respect to these rates of change. The model included a random intercept term to account for variation among animals within a given diet group in terms of the baseline level of the given outcome, and accounted for the lack of statistical independence among observations made on the same animal over time. The RCR analysis was also used to assess and compare the cuprizone groups in terms of the linear rate of change in outcome following the end of intoxication (recovery).

Trends in the EM measures were analyzed qualitatively.

Partial Spearman correlations were calculated between the MR and the relevant EM measures (MVF, mAWF, tAWF and *g*-ratio), using mouse weight at baseline as a covariate.

[1] http://imagej.nih.gov/ij/

A Pearson correlation was also computed between WMTI-derived AWF and EM-derived tAWF, as these two measures are meant to represent the same biophysical quantity.

All statistical tests were conducted at the two-sided 5% significance level using either SAS 9.3 (SAS Institute, Cary, NC) or Matlab.

3. Results

Figure 2A indicates the total number of animals per group and timepoint, for which MR data and EM data were available. Three animals from the Control group died accidentally during scanning, two at baseline and one at 6 weeks, and were excluded from the analysis. Figure 2B illustrates the animal weight in a group at each timepoint. Animals on cuprizone did not gain weight as fast as the control animals. Between 6 weeks and 12 weeks, Cpz6 animals recovered some weight compared to Cpz12 animals which were still on cuprizone.

3.1. Effect of cuprizone exposure and recovery on MR measures

Figure 3 shows representative parametric maps of MR metrics, as well as an outline of the splenium ROI. Since this work focuses on demyelination and remyelination, results are only presented for the diffusion measures potentially affected by changes in the *radial direction* (i.e. perpendicular to the main orientation of the axons): RD,[2] RK, AWF and $D_{e,\perp}$. Figure 4 highlights the significant differences between diet arms at a given timepoint (see Table 1 for exact *p*-values and Cohen's d) and Figure 5 the significant trends along time in a given diet group (see Supplementary Tables 1 and 2 for estimates of the linear rates of change in each measure, as well as the *p*-values for the comparison of rates between groups). ANCOVA and Cohen's d results for all MR metrics are available in Supplementary Table 3.

At 6 weeks, T_2 and RD were significantly higher (+13% and +21%, respectively), and MTR, RK and AWF significantly lower (-22%, -23% and -19%, respectively) in animals on cuprizone compared to controls ($p < 0.032$). $D_{e,\perp}$ also displayed the expected trend (+8%) but the difference was not significant ($p = 0.23$). Based on Cohen's d, T_2 values had the largest standardized difference between cuprizone and controls, followed by AWF and RD.

At 12 weeks, the Cpz12 mice further deteriorated relative to controls, with significant differences in terms of T_2 (+23%), RD (+34%), MTR (-30%), as well as AWF (-20%) and $D_{e,\perp}$ (+32%) ($p < 0.014$). Partial recovery in Cpz6 mice also was evident as metrics lay in-between values for Ctl and Cpz12 (see Figure 4). The differences between Cpz6 and Ctl were still significant only in terms of T_2 ($p = 0.0166$), and between Cpz6 and Cpz12 only in terms of RD and T_2 ($p \leq 0.021$).

At 18 weeks, the Cpz12 mice partially recovered compared to the 12 week timepoint, but MR measures in this group remained altered compared to Ctl (from +7% for $D_{e,\perp}$ and up to -38% for RK). The differences were only significant in MTR ($p = 0.029$), but the size of the groups at this timepoint (three Ctl and six Cpz12) also reduced statistical power.

[2]Changes in FA mirror changes in RD and are therefore only included in supplementary material, for simplicity.

In terms of initial linear rates of change, the control group displayed a significant decrease in T_2 and increase in MTR from baseline through 18 weeks ($p \leq 0.016$). This trend could be attributed to on-going development in the mice, but it was not found in the diffusion metrics. The Cpz6 group displayed a significant linear increase in T_2 and RD, and decrease in AWF and MTR from baseline to 6 weeks ($p \leq 0.027$), consistent with cuprizone-induced demyelination. There was a trend of increase in $D_{e,\perp}$ ($p = 0.062$). The Cpz12 group displayed the same linear changes as Cpz6, as well as a significant increase in $D_{e,\perp}$, from baseline to 12 weeks ($p \leq 0.009$), consistent with on-going cuprizone intoxication. Although the rates of change were systematically lower in Cpz12 compared to Cpz6, the difference between these rates was not significant ($p \geq 0.133$) (Supplementary Table 1). The rates of change in both Cpz6 and Cpz12 were significantly different from Ctl in all of the above mentioned measures ($p \leq 0.022$).

Opposite trends, consistent with recovery, were found for both Cpz6 (between 6 and 12 weeks) and Cpz12 (between 12 and 18 weeks), but they were only significant for T_2 and MTR in the Cpz12 group ($p \leq 0.029$) (Supplementary Table 2).

3.2. Effect of cuprizone exposure and recovery on EM measures

Figure 6 collects results from the quantitative analysis of EM images.

Myelin-related measures and *g*-ratio followed the expected trend with intoxication and recovery. At 6 weeks, the MVF and mAVF were lower (-12% and -6.5%, respectively) in Cpz6 than in Ctl, and the mAxCount was substantially lower (-35%) in Cpz6 relative to Ctl, which is indicative of demyelination and also of the preferential demyelination of smaller axons first (Mason et al., 2001; Thiessen et al., 2013). At 12 weeks, the difference was even larger between Cpz12 and Ctl (from +11% for *g*-ratio and up to -51% for MVF), with metrics for Cpz6 (after 6 weeks of recovery) lying in-between these two groups. The Cpz6 and Cpz12 groups showed recovery in these measures compared to their 6-week and 12-week timepoints, respectively. The metrics most sensitive to recovery were mAxCount (+21% in Cpz6 at 12 weeks compared to 6 weeks) and mAVF (+33% in Cpz12 at 18 weeks compared to 12 weeks).

The dynamics of the remaining measures, tAVF and tAxCount, were more complex. The differences in tAVF were within measurement error: tAVF seemed to be preserved overall in spite of the cuprizone diet. This observation is consistent with cuprizone inducing almost no axonal loss (Irvine and Blakemore, 2008; Skripuletz et al., 2011). However, tAxCount in Cpz6 and Cpz12 was surprisingly higher than in controls starting at 12 weeks (+35%). This is most likely due to chemical fixation (Boonstra et al., 1983; Wehrl et al., 2015), with a higher shrinkage factor for the extra-axonal space relative to the intra-axonal space. While the interpretation of our results relies on this explanation, other possible but less documented potential explanations involve *in vivo* filling of the extracellular space resulting from demyelination with neighboring axons, or on-going myelination in control animals. Indeed, tAxCount in the control group decreased between 6 and 12 weeks (-45%), which, alongside the increase in mAVF (+68%), could point to myelination; since myelinated axons are larger, they also induce a lower overall axon count per unit area of tissue.

3.3. Correlations between MR and EM measures

Table 2 summarizes the results of Spearman correlations between MR-derived and EM-derived measures of interest (see Supplementary Table 4 for correlations between all measures) and Figure 7 shows scatter plots for measures of particular interest. Conventional MR measures such as radial diffusivity and T_2 correlated very strongly ($|\rho| = 0.52 – 0.71$, $p < 0.02$) with EM-derived MVF, mAWF and *g*-ratio. MTR and radial kurtosis showed significant correlations with tAWF ($|\rho| = 0.49 – 0.56$, $p < 0.03$), but neither with *g*-ratio nor, surprisingly for MTR, with MVF ($p > 0.18$). Among WMTI metrics, the AWF correlated most strongly with tAWF ($\rho = 0.66$, $p = 0.0014$), followed by mAWF ($\rho = 0.61$, $p = 0.0046$) and MVF ($\rho = 0.55$, $p = 0.0112$); it did not correlate significantly with the *g*-ratio ($p > 0.08$). On the other hand, $D_{e,\perp}$ correlated most strongly with MVF ($\rho = -0.50$, $p = 0.026$) and *g*-ratio ($\rho = 0.48$, $p = 0.0342$); it did not correlate significantly with mAWF and tAWF ($p > 0.13$).

The Pearson correlation between WMTI-derived AWF and EM-derived tAWF was also significant ($\rho = 0.60$, $p = 0.0053$). The linear regression between these two quantities was characterized by an intercept of (0.014 ± 0.120) and a slope of (0.58 ± 0.17).

4. Discussion

In this work, we investigated the performance of various MR measures to monitor cuprizone-induced demyelination and subsequent recovery: from conventional measures to more specific ones, such as WMTI-derived axonal water fraction and extra-axonal radial diffusivity. The changes observed *in-vivo* were consistent with those obtained from quantitative EM image analysis. Using animals for which both MR and EM examinations were available, we measured several significant correlations between the non-invasive MR metrics and various microstructural tissue characteristics derived from EM. The correlations revealed a potentially useful differentiation between the WMTI-derived AWF on the one hand, and $D_{e,\perp}$ on the other.

4.1. *Ex vivo* microstructural imaging of splenium during cuprizone intoxication and recovery

The metrics derived from EM images were consistent with expected trends of cuprizone intoxication and recovery (Lindner et al., 2008; Steelman et al., 2012; Stidworthy et al., 2003; Xie et al., 2010). The measure most sensitive to acute intoxication and subsequent recovery was mAxCount. Following chronic intoxication, MVF, mAVF and mAxCount were all dramatically reduced compared to control levels. The effect of subsequent recovery was most readily observed as an increase in mAVF and mAxCount.

Importantly, our measures were quantitatively consistent with previous EM analyses from the literature. At six weeks, our control group was characterized by 26% myelinated axons, 19% myelin fraction and 30% unmyelinated axons, whereas (Thiessen et al., 2013) reported: 30% myelinated axons, 28% myelin fraction and 41% non-myelinated cells (axons, glial processes, etc). The effect of cuprizone treatment was more drastic in the latter work, consistent with the higher concentration administered (0.4% vs. 0.2% here). Similarly, the

mAxCount in our control group at 6 weeks (1.2×10^6 per mm^2) compared well with that reported by (Steelman et al., 2012) (1.25×10^6 per mm^2). In the latter work, the cuprizone insult was maintained at 0.2% for five weeks. At seven weeks, the mAxCount in the intoxicated group was 0.5×10^6 per mm^2, which also was comparable to, albeit somewhat lower than, our estimate of 0.77×10^6 per mm^2 at six weeks.

We chose to use transmission EM over histological staining and optical microscopy in order to access quantities with great neurological relevance such as the *g*-ratio, which dictates the conduction speed along the axon. Moreover, histological staining can potentially overestimate intact myelin content because of myelin debris. The latter are a complex confounding factor, especially as their amount varies in time, peaking at 6 weeks from intoxication and being cleared completely at 8 weeks upon recovery (Lindner et al., 2008; Matsushima and Morell, 2001). Importantly, the EM images (Figure 6A) confirmed a pattern of inhomogeneous, "patchy", demyelination over length scales of ~5 μm, also consistent with previous reports (Stidworthy et al., 2003). This pattern plays an important role in the interpretation of the WMTI findings, as discussed below.

4.2. *In vivo* MR monitoring of cuprizone intoxication and recovery, and correlation with EM

Conventional MR measures – T_2, MTR and RD – were sensitive to the effect of cuprizone intoxication and recovery at all timepoints, as previously also reported (Falangola et al., 2014; Song et al., 2005; Thiessen et al., 2013; Wu et al., 2008; Zaaraoui et al., 2008). Based on Cohen's d, T_2 was the best discriminator between controls and cuprizone-treated animals at all timepoints; RD was the best discriminator between Cpz6 and Cpz12 at 12 weeks.

RD and T_2 correlated strongly with all myelin-related EM metrics, which confirmed both their sensitivity and lack of specificity, also in agreement with previous findings (Gareau et al., 2000; Song et al., 2005; Wu et al., 2008). For example, an increase in RD can be caused by both demyelination and axonal loss (Klawiter et al., 2011).

MTR correlated with tAWF, but, surprisingly, not with MVF. While other works reported a significant correlation between MTR and either the amount of myelin basic protein (Zaaraoui et al., 2008) or MVF (Thiessen et al., 2013), it should be noted that, in the latter study, MTR also correlated significantly with the volume fraction of non-myelinated cells. The specificity of MTR is reputedly poor, with large sensitivity to inflammation and edema (Gareau et al., 2000; Vavasour et al., 2011). A recent study of demyelination by induction of experimental autoimmune encephalomyelitis in mice even found that changes in MTR did not correlate with myelin content, questioning the usefulness of MTR as a surrogate marker for demyelination in that mouse model (Fjaer et al., 2015). Quantitative magnetization transfer studies reported a strong correlation between the measured bound pool fraction *F* and the myelin fraction, with potentially improved specificity (Thiessen et al., 2013; Turati et al., 2015). However, while providing useful information on the overall myelin content, magnetization transfer-based techniques, as T_2 based techniques, are less sensitive to the functional integrity of the myelin as might be reflected by sheath thickness, or the differentiation between intact myelin and debris.

In the present work, none of the measures related to diffusion along the fiber bundle (i.e. AK, AD, D_a or $D_{e,\parallel}$) was significantly different between diet groups, or correlated with EM-derived myelin measures (Supplementary Tables 3 and 4). These negative results are consistent with a pattern of demyelination inducing diffusion changes in the radial direction mainly. However, radial kurtosis was not sensitive to cuprizone intoxication and neither recovery, and only correlated with tAWF. We note that, in the context of this work, MK was in fact a better discriminator between diet groups than RK (Supplementary Table 3). This is likely related to the larger sensitivity of RK (relative to the other diffusion metrics) to noise and Gibbs ringing in structures characterized by low RD (Veraart et al., 2015). Indeed, an unfortunate combination of underlying low (though positive) diffusion and noise and/or Gibbs ringing can produce highly negative kurtosis values. However, because constraints are enforced in the tensor fit ($K \geq 0$), the diffusion directions for which this scenario occurs will still be attributed positive – often very close to zero, but likely unreliable – kurtosis values. These values might interfere with the statistical analysis, mainly being a source of increased variability within an ROI. In contrast, a previous study of DKI and WMTI changes with cuprizone diet showed all kurtosis metrics (MK, RK, and also AK) as well as $D_{e,\parallel}$ to differentiate between controls and cuprizone animals at 10 weeks into intoxication, and AD, AK and D_a to correlate with Solochrome myelin staining (Falangola et al., 2014). This different observation could be explained by the different timing of experiments: while ours were carried out at 6 and 12 weeks, those in Falangola *et al.* were at 10 weeks, when the level of microglia is peaking prior to the new partial remyelination known to occur at 12 weeks (Matsushima and Morell, 2001). Thus, the effects they measured in axial diffusion metrics, and by the same reasoning potentially radial kurtosis, could be related to the crowding of the extra-axonal space by macrophages and microglia. It should be noted that although astrogliosis is known to persist at the timepoints imaged in the current study (6 and 12 weeks), its potential effect on axial metrics (AD, AK, D_a or $D_{e,\parallel}$) has not been found significant.

In terms of AWF and $D_{e,\perp}$, their dynamics with intoxication were different from each other, thus providing complementary information. At six weeks, AWF was significantly reduced in the cuprizone animals compared to controls, while the increase in $D_{e,\perp}$ was not significant. By 12 weeks, AWF and $D_{e,\perp}$ in Cpz12 were both significantly different from controls. The magnitude effect was however now more pronounced in $D_{e,\perp}$ (+32%) than in AWF (-20%).

A possible explanation for the more limited involvement of $D_{e,\perp}$ at 6 weeks, could be found in the observation that cuprizone-induced demyelination is not homogeneous, but rather “patchy”, as seen on the EM images (Figure 6A) and also documented in the literature (Stidworthy et al., 2003). Previous simulations suggested the impact of random axonal loss is initially large on AWF and limited on $D_{e,\perp}$, while that of uniform demyelination is initially large on $D_{e,\perp}$ and limited on AWF (Novikov and Fieremans, 2012). From the perspective of molecule mobility, patchy demyelination is comparable to axonal loss if the diffusion distance is greater than the typical size of the patch. We estimated a patch size of $\sim$5 μm and a diffusion distance of 8 μm in the transverse plane, assuming diffusivity $D = 1$ μm^2/ms and diffusion time $t = 16$ ms. Hence, while diffusion may be less restricted in the patch itself due to increased extra-axonal space, it is still restricted over the total diffusion distance to a similar extent as the control case, due to the overall presence of intact

myelinated axons. Therefore, this demyelination pattern impacted $D_{e,\perp}$ to a lesser extent than AWF.

The correlations between EM and WMTI metrics also support the specificity associated with AWF and $D_{e,\perp}$ as expected from the WMTI model. AWF correlated with mAWF and tAWF, while $D_{e,\perp}$ did not. Conversely, the correlation between $D_{e,\perp}$ and g-ratio was significant, while that between AWF and g-ratio was not (although a trend was present). It should be noted that Kelm and colleagues reported no linear correlation between $D_{e,\perp}$ and myelin metrics extracted from EM in a mouse model of hypomyelination (Kelm et al., 2016). We stress however that there is likely a packing difference between myelinated axons that have become demyelinated and axons that were never myelinated. Moreover, Kelm et al. did not account for unmyelinated axons in their EM analysis, which could also explain the difference in outcomes.

The WMTI-derived AWF and the EM-derived tAWF are by design measures of the same biophysical quantity. Indeed, the cellular membrane itself, with or without myelin, restricts diffusion (Beaulieu and Allen, 1994), especially for the diffusion times employed here (16 ms), whereby the intra-axonal space is the collection of all axons, not only of myelinated ones. Remarkably, these two measures correlated very strongly and their relationship was well fit by a linear model with negligible intercept: $AWF_{WMTI} \approxeq 0.58 \cdot tAWF_{EM} + 0.014$. The slope however was not unity, indicative of a scaling effect between the two modalities. One explanation for this scaling could be non-linear shrinkage caused by chemical fixation in the EM images: the extra-axonal space shrank more than the intra-axonal space. Another explanation, this time affecting AWF_{WMTI}, could be a higher transverse relaxation rate in the intra- vs. the extra-axonal space which would introduce a non-negligible $e^{-TE \cdot \Delta R_2}$ weighting.

4.3. Limitations

While mice 8-10 weeks old are a standard choice for cuprizone studies (Skripuletz et al., 2011), which also guided our choice for this study, the age of “adulthood” in mice is not firmly established, with reports ranging from 8 weeks old for atlases of “adult mouse brain” (Lein et al., 2007), to 3 – 6 months as the age range for mature adults (Flurkey et al., 2007). Some results in the current work, such as the significant decrease in T_2 and increase in MTR in the control animals over the 18 weeks of follow-up, suggest that there might have been ongoing development in the control group over the course of the study. This may have acted as a confounding factor. It should also be noted that, unfortunately, most previous longitudinal cuprizone studies reported control values at baseline only (typically 8 weeks of age, like in our study) and used them as a reference for values in the intoxicated animals at later timepoints. In the present work, values from the Cpz6 or Cpz12 groups were compared to values in controls at the same timepoint, which, in the light of our observations on control mice from this strain, was likely more appropriate and hopefully limited the confound related to development. However, for future studies, we would recommend working with mice at least 18 weeks old at baseline.

A second potential confounding factor stems from establishing a comparison between MR metrics averaged over an entire ROI of $\sim$0.1 mm^3 and EM metrics averaged over 8 images

of ∼50 μm^2 and a few nm thick each. It should also be noted that we assumed invariance of structures along the direction of the fibers when deriving volume fractions from 2D cross-sectional EM images. However, we tried to minimize this confound by analyzing 8 different images randomly distributed across the splenium sample, which on average could be reasonably representative of the entire structure. We stress that the EM measures are likely biased, since the EM samples are altered by fixation and tissue preparation. Our aim was therefore not to use EM images as "ground truth" for validation of *in vivo* measures, but rather to test for correlations between the two modalities. The correlations found between MR and EM measures were very strong and fully consistent with biophysical assumptions.

The correlations between MR and EM were performed using all available mice, irrespective of their diet group. While it would be ideal to assess correlations within each diet group separately, this was not possible given the sample sizes. However, the various durations of cuprizone intoxication and recovery served to introduce the necessary range in each measure for a correlation to be established; it is noteworthy that the control and intoxicated animals do not lie in entirely disconnected regions of parameter space but form a continuous distribution. The establishment of separate correlations between MR and EM measures for each diet group would be highly insightful and could be the subject of future work involving a larger sample size.

In addition, changes in EM metrics between timepoints should be interpreted with caution since, unlike MRI, there can be no longitudinal follow-up in EM, and statistics for a given group are established based on different animals at each timepoint.

Finally, as mentioned in the Introduction, certain assumptions underlie the WMTI model which may limit its applicability. In particular, it assumes that $D_a \leq D_{e,\parallel}$ and is only valid in regions of limited fiber orientation dispersion. Both of these assumptions are about to be lifted in the near future, by employing the recent approaches based on rotational invariants (such as the LEMONADE method utilizing diffusion signal moments (Novikov et al., 2015)), that are able to separate the estimation of any fiber orientation distribution function from that of compartment diffusivities and fractions. These methods are thus applicable to any brain region and their performance is currently being evaluated.

4.4 Perspectives

This longitudinal study aimed to track microstructural changes at major timepoints over a long course of cuprizone intoxication and recovery. However, establishing more detailed parameter dynamics during the first six weeks of cuprizone intoxication could also be insightful. For example, the three week timepoint is characterized by early demyelination and inflammation, and the five week by peak inflammatory response and start of spontaneous remyelination (Matsushima and Morell, 2001). Recent work by (Guglielmetti et al., 2016) examined the three week timepoint and showed that, in the splenium, it was characterized by a marked decrease in D_a, attributed to axonal swelling or beading as a result of severe microglial activation and myelin breakdown. Future work should focus on further establishing the sensitivity and specificity of compartment diffusion parameters to changes at these earlier stages, also relying on EM for validation.

In the current study, T_2 displayed the highest sensitivity to cuprizone-induced changes, and WMTI parameters AWF and $D_{e,\perp}$ the highest specificity to the gradual steps of changes. A combination of T_2 and multi-shell diffusion acquisitions therefore seems most promising for routine monitoring of microstructural changes.

From a broader perspective, the specificity of *in vivo* biomarkers is arguably most important in a clinical context. In animal experiments, one has very good control over the inflicted injury and/or pathology. In patients however, the pathology is not known *a priori*, and/or the underlying microstructural changes of the tissue are poorly understood. Various pathological changes can have similar signatures in terms of unspecific biomarkers such as FA or RD. Yet, from a therapeutic point of view, patchy demyelination, widespread demyelination, axonal loss, inflammation, etc. should likely be approached differently. The accurate identification of disease mechanisms *in vivo* is therefore crucial to the development of appropriate therapy. Improved diagnostic tools today will undoubtedly benefit the therapeutic approaches and patient management of tomorrow.

5. Conclusions

WMTI model parameters are promising candidates as sensitive and specific biomarkers of demyelination and remyelination in the white matter. The acute intoxication (6 weeks of cuprizone) produced a significant decrease in AWF, with only mild changes in $D_{e,\perp}$, consistent with patchy demyelination. The chronic intoxication (12 weeks of cuprizone) caused a more marked increase in $D_{e,\perp}$, consistent with more severe demyelination and clearance of the extra-axonal space. Remyelination produced the expected reversal in trends. The specificities of these parameters were further supported by their respective correlations with EM-derived microstructural features. The WMTI-derived axonal water fraction correlated with both EM-derived myelinated and total axonal water fraction, but not with the *g*-ratio, while $D_{e,\perp}$ correlated with the *g*-ratio but not with the EM-derived axonal water fractions. We stress that the WMTI model is based on data that can be acquired in less than five minutes on current clinical scanners and is thus easily applicable clinically. WMTI therefore has great potential for routine monitoring of microstructural changes in the major white matter tracts affected by demyelinating pathologies.

Supplementary Material

Refer to Web version on PubMed Central for supplementary material.

Acknowledgments

The authors would like to acknowledge technical assistance from the Microscopy Core of New York University Langone Medical Center. This study was supported in part by grants R21 NS081230 and R01 NS088040 from the NINDS (NIH), by grant UL1 TR00038 from the NCATS, by the Raymond and Beverly Sackler Laboratories for the Convergence of Biomedical, Physical, and Engineering Sciences, and by the Center of Advanced Imaging Innovation and Research (CAI2R, www.cai2r.net), a NIBIB Biomedical Technology Resource Center: P41 EB017183.

References

Aggarwal M, Mori S, Shimogori T, Blackshaw S, Zhang J. Three-dimensional diffusion tensor microimaging for anatomical characterization of the mouse brain. Magn Reson Med. 2010; 64:249–261. [PubMed: 20577980]

Beaulieu C, Allen PS. Water diffusion in the giant axon of the squid: implications for diffusion-weighted MRI of the nervous system. Magn Reson Med. 1994; 32:579–583. [PubMed: 7808259]

Benitez A, Fieremans E, Jensen JH, Falangola MF, Tabesh A, Ferris SH, Helpern JA. White matter tract integrity metrics reflect the vulnerability of late-myelinating tracts in Alzheimer's disease. Neuroimage Clin. 2013; 4:64–71. [PubMed: 24319654]

Boonstra H, Oosterhuis JW, Oosterhuis AM, Fleuren GJ. Cervical tissue shrinkage by formaldehyde fixation, paraffin wax embedding, section cutting and mounting. Virchows Arch A Pathol Anat Histopathol. 1983; 402:195–201. [PubMed: 6420986]

Brun A, Englund E. A white matter disorder in dementia of the Alzheimer type: a pathoanatomical study. Ann Neurol. 1986; 19:253–262. [PubMed: 3963770]

Collier Q, Veraart J, Jeurissen B, den Dekker AJ, Sijbers J. Iterative reweighted linear least squares for accurate, fast, and robust estimation of diffusion magnetic resonance parameters. Magn Reson Med. 2015; 73:2174–2184. [PubMed: 24986440]

Davis KL, Stewart DG, Friedman JI, Buchsbaum M, Harvey PD, Hof PR, Buxbaum J, Haroutunian V. White matter changes in schizophrenia: evidence for myelin-related dysfunction. Arch Gen Psychiatry. 2003; 60:443–456. [PubMed: 12742865]

Falangola MF, Guilfoyle DN, Tabesh A, Hui ES, Nie X, Jensen JH, Gerum SV, Hu C, LaFrancois J, Collins HR, Helpern JA. Histological correlation of diffusional kurtosis and white matter modeling metrics in cuprizone-induced corpus callosum demyelination. NMR Biomed. 2014; 27:948–957. [PubMed: 24890981]

Fieremans E, Benitez A, Jensen JH, Falangola MF, Tabesh A, Deardorff RL, Spampinato MV, Babb JS, Novikov DS, Ferris SH, Helpern JA. Novel white matter tract integrity metrics sensitive to Alzheimer disease progression. AJNR Am J Neuroradiol. 2013; 34:2105–2112. [PubMed: 23764722]

Fieremans E, Jensen JH, Helpern JA. White matter characterization with diffusional kurtosis imaging. Neuroimage. 2011; 58:177–188. [PubMed: 21699989]

Fieremans, E.; Jensen, JH.; Helpern, JA.; Kim, S.; Grossman, RI.; Inglese, M.; Novikov, DS. Proc Intl Soc Magn Reson Med. Vol. 20. Melbourne, Australia: 2012. Diffusion distinguishes between axonal loss and demyelination in brain white matter.

Fieremans E, Novikov DS, Jensen JH, Helpern JA. Monte Carlo study of a two-compartment exchange model of diffusion. NMR Biomed. 2010; 23:711–724. [PubMed: 20882537]

Filippi M, Preziosa P, Rocca MA. Magnetic resonance outcome measures in multiple sclerosis trials: time to rethink? Curr Opin Neurol. 2014; 27:290–299. [PubMed: 24792339]

Fjaer S, Bo L, Myhr KM, Torkildsen O, Wergeland S. Magnetization transfer ratio does not correlate to myelin content in the brain in the MOG-EAE mouse model. Neurochem Int. 2015; 83-84:28–40. [PubMed: 25744931]

Flurkey, K.; Currer, JM.; Harrison, DE. The Mouse in Aging Research. In: Fox, JGea, editor. The Mouse in Biomedical Research. Elsevier; Burlington, MA: 2007. p. 637-672.

Galvin RJ, Regan D, Heron JR. A possible means of monitoring the progress of demyelination in multiple sclerosis: effect of body temperature on visual perception of double light flashes. J Neurol Neurosurg Psychiatry. 1976; 39:861–865. [PubMed: 993807]

Gareau PJ, Rutt BK, Karlik SJ, Mitchell JR. Magnetization transfer and multicomponent T2 relaxation measurements with histopathologic correlation in an experimental model of MS. J Magn Reson Imaging. 2000; 11:586–595. [PubMed: 10862056]

Grossman EJ, Kirov II, Gonen O, Novikov DS, Davitz MS, Lui YW, Grossman RI, Inglese M, Fieremans E. N-acetyl-aspartate levels correlate with intra-axonal compartment parameters from diffusion MRI. Neuroimage. 2015; 118:334–343. [PubMed: 26037050]

Grossman RI, McGowan JC. Perspectives on multiple sclerosis. AJNR Am J Neuroradiol. 1998; 19:1251–1265. [PubMed: 9726464]

Guglielmetti C, Veraart J, Roelant E, Mai Z, Daans J, Van Audekerke J, Naeyaert M, Vanhoutte G, Delgado y Palacios R, Praet J, Fieremans E, Ponsaerts P, Sijbers J, Van der Linden A, Verhoye M. Diffusion kurtosis imaging probes cortical alterations and white matter pathology following cuprizone induced demyelination and spontaneous remyelination. Neuroimage. 2016; 125:363–377. [PubMed: 26525654]

Hommes OR. Remyelination in human CNS lesions. Prog Brain Res. 1980; 53:39–63. [PubMed: 7005954]

Hui ES, Fieremans E, Jensen JH, Tabesh A, Feng W, Bonilha L, Spampinato MV, Adams R, Helpern JA. Stroke assessment with diffusional kurtosis imaging. Stroke. 2012; 43:2968–2973. [PubMed: 22933581]

Irvine KA, Blakemore WF. Remyelination protects axons from demyelination-associated axon degeneration. Brain. 2008; 131:1464–1477. [PubMed: 18490361]

Jelescu IO, Veraart J, Adisetiyo V, Milla SS, Novikov DS, Fieremans E. One diffusion acquisition and different white matter models: How does microstructure change in human early development based on WMTI and NODDI? Neuroimage. 2015; 107:242–256. [PubMed: 25498427]

Jelescu IO, Veraart J, Fieremans E, Novikov DS. Degeneracy in model parameter estimation for multicompartmental diffusion in neuronal tissue. NMR Biomed. 2016; 29:33–47. [PubMed: 26615981]

Jenkinson M, Bannister P, Brady M, Smith S. Improved optimization for the robust and accurate linear registration and motion correction of brain images. Neuroimage. 2002; 17:825–841. [PubMed: 12377157]

Jenkinson M, Smith S. A global optimisation method for robust affine registration of brain images. Med Image Anal. 2001; 5:143–156. [PubMed: 11516708]

Jensen JH, Helpern JA, Ramani A, Lu H, Kaczynski K. Diffusional kurtosis imaging: the quantification of non-gaussian water diffusion by means of magnetic resonance imaging. Magn Reson Med. 2005; 53:1432–1440. [PubMed: 15906300]

Kelm ND, West KL, Carson RP, Gochberg DF, Ess KC, Does MD. Evaluation of diffusion kurtosis imaging in ex vivo hypomyelinated mouse brains. Neuroimage. 2016; 124:612–626. [PubMed: 26400013]

Kinnunen KM, Greenwood R, Powell JH, Leech R, Hawkins PC, Bonnelle V, Patel MC, Counsell SJ, Sharp DJ. White matter damage and cognitive impairment after traumatic brain injury. Brain. 2011; 134:449–463. [PubMed: 21193486]

Klawiter EC, Schmidt RE, Trinkaus K, Liang HF, Budde MD, Naismith RT, Song SK, Cross AH, Benzinger TL. Radial diffusivity predicts demyelination in ex vivo multiple sclerosis spinal cords. Neuroimage. 2011; 55:1454–1460. [PubMed: 21238597]

Klein S, Staring M, Murphy K, Viergever MA, Pluim JP. elastix: a toolbox for intensity-based medical image registration. IEEE Trans Med Imaging. 2010; 29:196–205. [PubMed: 19923044]

Lamantia AS, Rakic P. Cytological and quantitative characteristics of four cerebral commissures in the rhesus monkey. Journal of Comparative Neurology. 1990; 291:520–537. [PubMed: 2329189]

Lamprecht MR, Sabatini DM, Carpenter AE. CellProfiler: free, versatile software for automated biological image analysis. Biotechniques. 2007; 42:71–75. [PubMed: 17269487]

Lazar M, Miles LM, Babb JS, Donaldson JB. Axonal deficits in young adults with High Functioning Autism and their impact on processing speed. Neuroimage Clin. 2014; 4:417–425. [PubMed: 24624327]

Lein ES, Hawrylycz MJ, Ao N, Ayres M, Bensinger A, Bernard A, Boe AF, Boguski MS, Brockway KS, Byrnes EJ, Chen L, Chen L, Chen TM, Chin MC, Chong J, Crook BE, Czaplinska A, Dang CN, Datta S, Dee NR, Desaki AL, Desta T, Diep E, Dolbeare TA, Donelan MJ, Dong HW, Dougherty JG, Duncan BJ, Ebbert AJ, Eichele G, Estin LK, Faber C, Facer BA, Fields R, Fischer SR, Fliss TP, Frensley C, Gates SN, Glattfelder KJ, Halverson KR, Hart MR, Hohmann JG, Howell MP, Jeung DP, Johnson RA, Karr PT, Kawal R, Kidney JM, Knapik RH, Kuan CL, Lake JH, Laramee AR, Larsen KD, Lau C, Lemon TA, Liang AJ, Liu Y, Luong LT, Michaels J, Morgan JJ, Morgan RJ, Mortrud MT, Mosqueda NF, Ng LL, Ng R, Orta GJ, Overly CC, Pak TH, Parry SE, Pathak SD, Pearson OC, Puchalski RB, Riley ZL, Rockett HR, Rowland SA, Royall JJ, Ruiz MJ, Sarno NR, Schaffnit K, Shapovalova NV, Sivisay T, Slaughterbeck CR, Smith SC, Smith KA,

Smith BI, Sodt AJ, Stewart NN, Stumpf KR, Sunkin SM, Sutram M, Tam A, Teemer CD, Thaller C, Thompson CL, Varnam LR, Visel A, Whitlock RM, Wohnoutka PE, Wolkey CK, Wong VY, Wood M, Yaylaoglu MB, Young RC, Youngstrom BL, Yuan XF, Zhang B, Zwingman TA, Jones AR. Genome-wide atlas of gene expression in the adult mouse brain. Nature. 2007; 445:168–176. [PubMed: 17151600]

Lindner M, Heine S, Haastert K, Garde N, Fokuhl J, Linsmeier F, Grothe C, Baumgartner W, Stangel M. Sequential myelin protein expression during remyelination reveals fast and efficient repair after central nervous system demyelination. Neuropathol Appl Neurobiol. 2008; 34:105–114. [PubMed: 17961136]

Mason JL, Langaman C, Morell P, Suzuki K, Matsushima GK. Episodic demyelination and subsequent remyelination within the murine central nervous system: changes in axonal calibre. Neuropathol Appl Neurobiol. 2001; 27:50–58. [PubMed: 11299002]

Matsushima GK, Morell P. The neurotoxicant, cuprizone, as a model to study demyelination and remyelination in the central nervous system. Brain Pathol. 2001; 11:107–116. [PubMed: 11145196]

Novikov, DS.; Fieremans, E. Proc Intl Soc Mag Reson Med. Vol. 20. Melbourne, Australia: 2012. Relating extracellular diffusivity to cell size distribution and packing density as applied to white matter; p. 1829

Novikov, DS.; Jelescu, IO.; Fieremans, E. Proc Intl Soc Mag Reson Med. Vol. 23. Toronto, Canada: 2015. From diffusion signal moments to neurite diffusivities, volume fraction and orientation distribution: An exact solution; p. 469

Oshio K, Feinberg DA. GRASE (Gradient- and spin-echo) imaging: a novel fast MRI technique. Magn Reson Med. 1991; 20:344–349. [PubMed: 1775061]

Praet J, Guglielmetti C, Berneman Z, Van der Linden A, Ponsaerts P. Cellular and molecular neuropathology of the cuprizone mouse model: Clinical relevance for multiple sclerosis. Neuroscience & Biobehavioral Reviews. 2014; 47:485–505. [PubMed: 25445182]

Skripuletz T, Gudi V, Hackstette D, Stangel M. De- and remyelination in the CNS white and grey matter induced by cuprizone: the old, the new, and the unexpected. Histol Histopathol. 2011; 26:1585–1597. [PubMed: 21972097]

Skripuletz T, Lindner M, Kotsiari A, Garde N, Fokuhl J, Linsmeier F, Trebst C, Stangel M. Cortical demyelination is prominent in the murine cuprizone model and is strain-dependent. Am J Pathol. 2008; 172:1053–1061. [PubMed: 18349131]

Song SK, Yoshino J, Le TQ, Lin SJ, Sun SW, Cross AH, Armstrong RC. Demyelination increases radial diffusivity in corpus callosum of mouse brain. Neuroimage. 2005; 26:132–140. [PubMed: 15862213]

Steelman AJ, Thompson JP, Li J. Demyelination and remyelination in anatomically distinct regions of the corpus callosum following cuprizone intoxication. Neurosci Res. 2012; 72:32–42. [PubMed: 22015947]

Stidworthy MF, Genoud S, Suter U, Mantei N, Franklin RJ. Quantifying the early stages of remyelination following cuprizone-induced demyelination. Brain Pathol. 2003; 13:329–339. [PubMed: 12946022]

Thiessen JD, Zhang Y, Zhang H, Wang L, Buist R, Del Bigio MR, Kong J, Li XM, Martin M. Quantitative MRI and ultrastructural examination of the cuprizone mouse model of demyelination. NMR Biomed. 2013; 26:1562–1581. [PubMed: 23943390]

Tomioka R, Matsui M. Biomarkers for multiple sclerosis. Intern Med. 2014; 53:361–365. [PubMed: 24583421]

Turati L, Moscatelli M, Mastropietro A, Dowell NG, Zucca I, Erbetta A, Cordiglieri C, Brenna G, Bianchi B, Mantegazza R, Cercignani M, Baggi F, Minati L. In vivo quantitative magnetization transfer imaging correlates with histology during de- and remyelination in cuprizone-treated mice. NMR Biomed. 2015; 28:327–337. [PubMed: 25639498]

Vavasour IM, Laule C, Li DK, Traboulsee AL, MacKay AL. Is the magnetization transfer ratio a marker for myelin in multiple sclerosis? J Magn Reson Imaging. 2011; 33:713–718. [PubMed: 21563257]

Veraart J, Fieremans E, Jelescu IO, Knoll F, Novikov DS. Gibbs ringing in diffusion MRI. Magn Reson Med. 201510.1002/mrm.25866

Veraart J, Sijbers J, Sunaert S, Leemans A, Jeurissen B. Weighted linear least squares estimation of diffusion MRI parameters: strengths, limitations, and pitfalls. Neuroimage. 2013; 81:335–346. [PubMed: 23684865]

Wehrl HF, Bezrukov I, Wiehr S, Lehnhoff M, Fuchs K, Mannheim JG, Quintanilla-Martinez L, Kohlhofer U, Kneilling M, Pichler BJ, Sauter AW. Assessment of murine brain tissue shrinkage caused by different histological fixatives using magnetic resonance and computed tomography imaging. Histol Histopathol. 2015; 30:601–613. [PubMed: 25504583]

Wu QZ, Yang Q, Cate HS, Kemper D, Binder M, Wang HX, Fang K, Quick MJ, Marriott M, Kilpatrick TJ, Egan GF. MRI identification of the rostral-caudal pattern of pathology within the corpus callosum in the cuprizone mouse model. J Magn Reson Imaging. 2008; 27:446–453. [PubMed: 17968901]

Xie M, Tobin JE, Budde MD, Chen CI, Trinkaus K, Cross AH, McDaniel DP, Song SK, Armstrong RC. Rostrocaudal analysis of corpus callosum demyelination and axon damage across disease stages refines diffusion tensor imaging correlations with pathological features. J Neuropathol Exp Neurol. 2010; 69:704–716. [PubMed: 20535036]

Zaaraoui W, Deloire M, Merle M, Girard C, Raffard G, Biran M, Inglese M, Petry KG, Gonen O, Brochet B, Franconi JM, Dousset V. Monitoring demyelination and remyelination by magnetization transfer imaging in the mouse brain at 9.4 T. MAGMA. 2008; 21:357–362. [PubMed: 18779984]

Abbreviations

AWF	axonal water fraction
DKI	diffusion kurtosis imaging
DTI	diffusion tensor imaging
EM	electron microscopy
FA	fractional anisotropy
mAVF	myelinated axonal volume fraction
mAWF	myelinated axonal water fraction
MD/AD/RD	mean-/axial-/radial diffusivity
MK/AK/RK	mean-/axial-/radial kurtosis
MTR	magnetization transfer ratio
MVF	myelin volume fraction
ROI	region of interest
tAVF	total axonal volume fraction
tAWF	total axonal water fraction
WMTI	white matter tract integrity

Highlights

- We monitored de- and remyelination with compartment-specific diffusion MRI metrics
- Axonal water fraction decreased with patchy demyelination (6 weeks of cuprizone)
- Extra-axonal radial diffusivity increased with widespread demyelination (12 weeks)
- Correlations with electron microscopy supported each metric's specificity
- These metrics are promising candidates as clinical biomarkers of demyelination

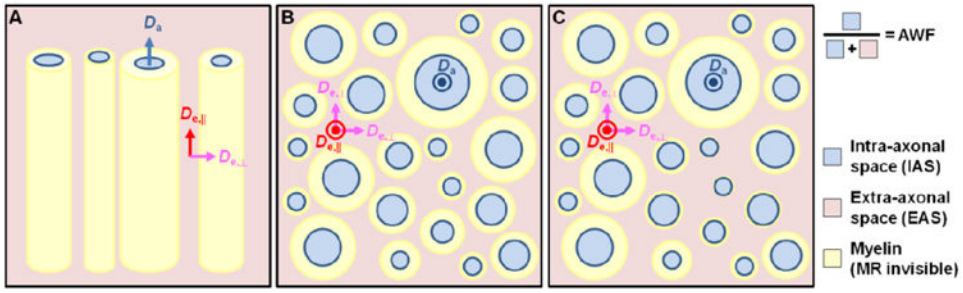

Figure 1.

The WMTI model for compartment specific water diffusivities. The compartments are color-coded, and axial (A) and transverse (B) views of the white matter bundle illustrate axial intra-axonal (D_a), axial extra-axonal ($D_{e,\parallel}$) and radial extra-axonal ($D_{e,\perp}$) diffusivities. Panel C illustrates a case of patchy demyelination, typical of cuprizone intoxication. Demyelination leads to an increase in extra-axonal space, which in turn causes an indirect decrease in AWF. If the characteristic size of the patch is shorter than the diffusion distance, $D_{e,\perp}$ will be minimally impacted. If the demyelination is widespread, $D_{e,\perp}$ will increase substantially.

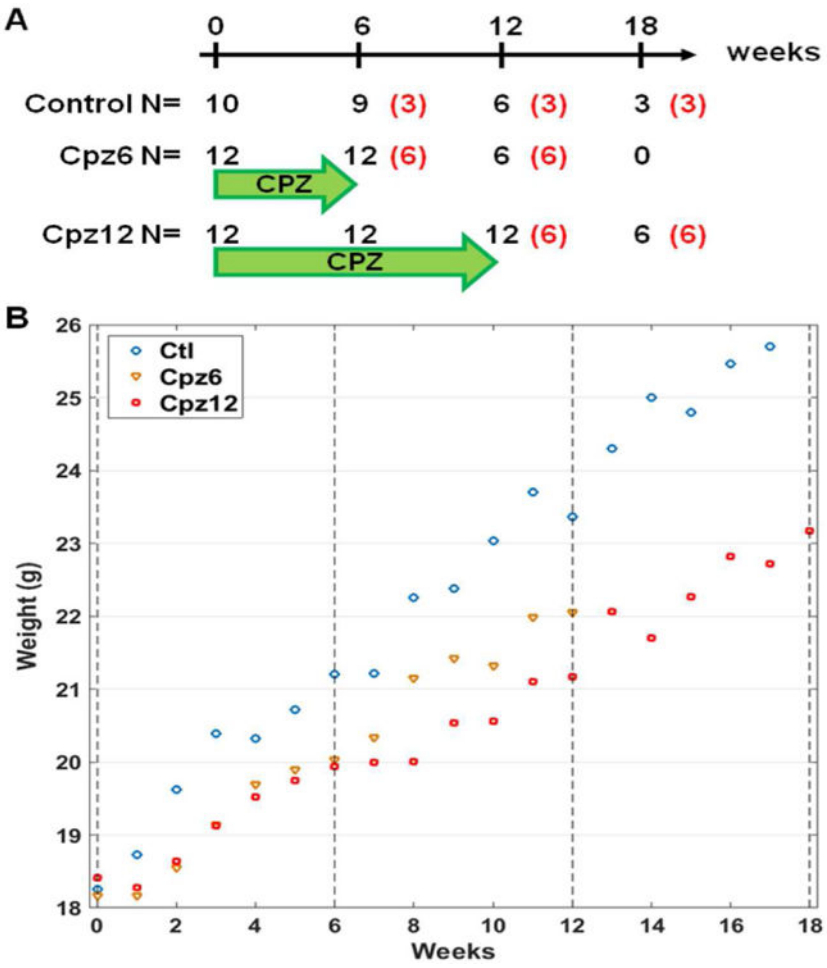

Figure 2.

A: Experimental timeline for number of *in-vivo* MR datasets (black) and *ex-vivo* EM (red, in brackets) per diet arm and timepoint. **B**: Mean mouse weight in each diet arm as a function of time.

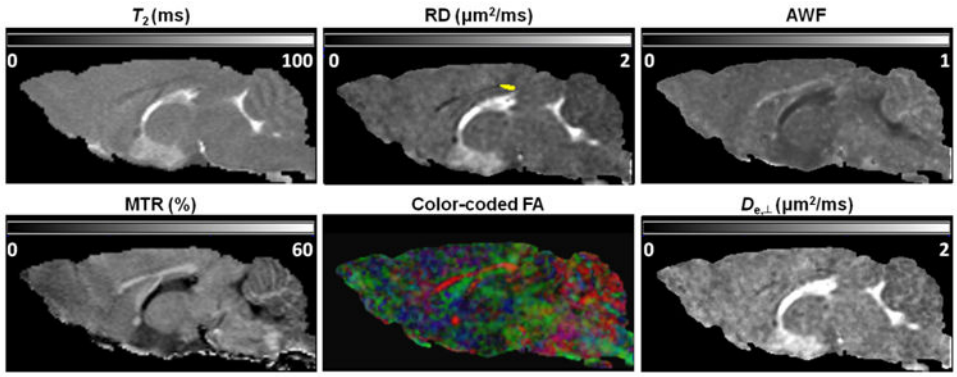

Figure 3.

Representative parametric maps of the MR measures relevant to this study, from a control animal at 18 weeks. The splenium ROI was drawn using the red channel of the color-coded FA map (red, green and blue colors correspond to the mediolateral, dorsoventral, and anterioposterior orientations, respectively) and is outlined in yellow on the RD map.

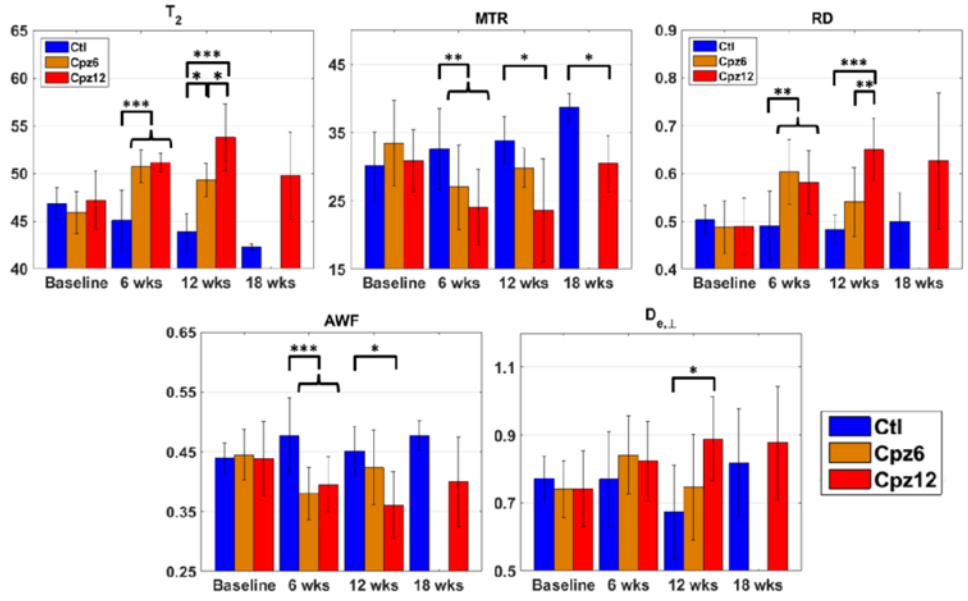

Figure 4.

Mean (± standard deviation) MR measures in each group, at each timepoint. Barplots highlight the differences between diet arms at a given timepoint - when significant (based on ANCOVA, see Table 1), the differences are marked with asterisks. *: $p < 0.05$; **: $p < 0.01$; ***: $p < 0.001$.

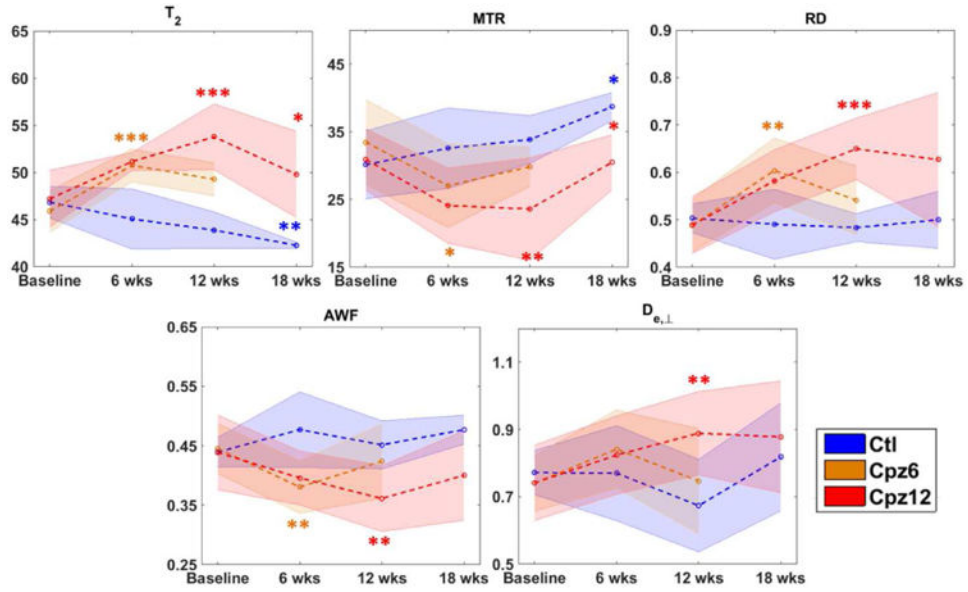

Figure 5.

Mean (± standard deviation) MR measures in each group, at each timepoint. Shaded plots highlight the trend along time in a given diet group. Linear trends during intoxication were assessed using RCR between baseline and 18 weeks for Ctl, baseline and 6 weeks for Cpz6, baseline and 12 weeks for Cpz12. Linear trends during recovery were assessed between 6 and 12 weeks for Cpz6, 12 and 18 weeks for Cpz12. Significant trends (see Supplementary Tables 1 and 2) are marked with asterisks at the final timepoint. *: $p < 0.05$; **: $p < 0.01$; ***: $p < 0.001$.

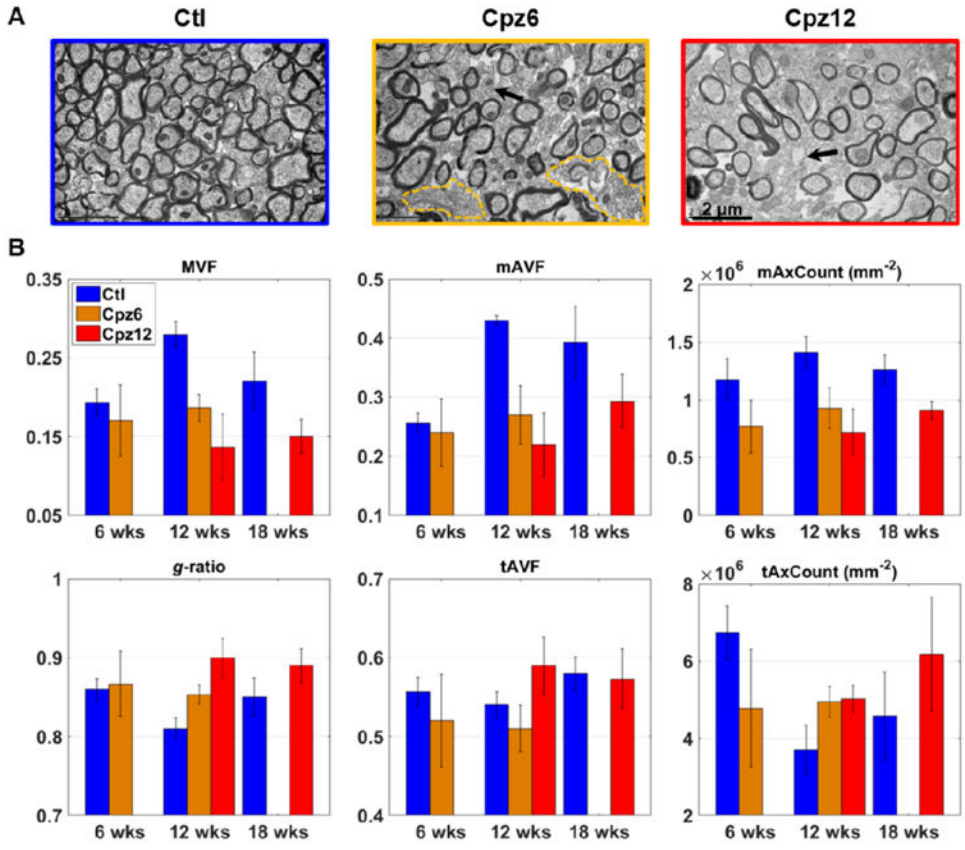

Figure 6.

Differences in diet arms from EM images. **A**: Representative EM images from each diet arm at the 12-week timepoint. The demyelination in Cpz12 is very advanced, while Cpz6 is partially remyelinated after 6 weeks of recovery. Black arrows point to examples of demyelinated axons, and dotted contours highlight areas of remaining patchy demyelination. **B**: Mean (± standard deviation) of EM measures, per group and timepoint. Myelin-related metrics (top row) and *g*-ratio follow the expected trend with intoxication and recovery. Total AVF and total axonal count seem to be preserved or even higher in cuprizone vs. control animals - this trend is likely artifactual and related to the shrinkage of structures.

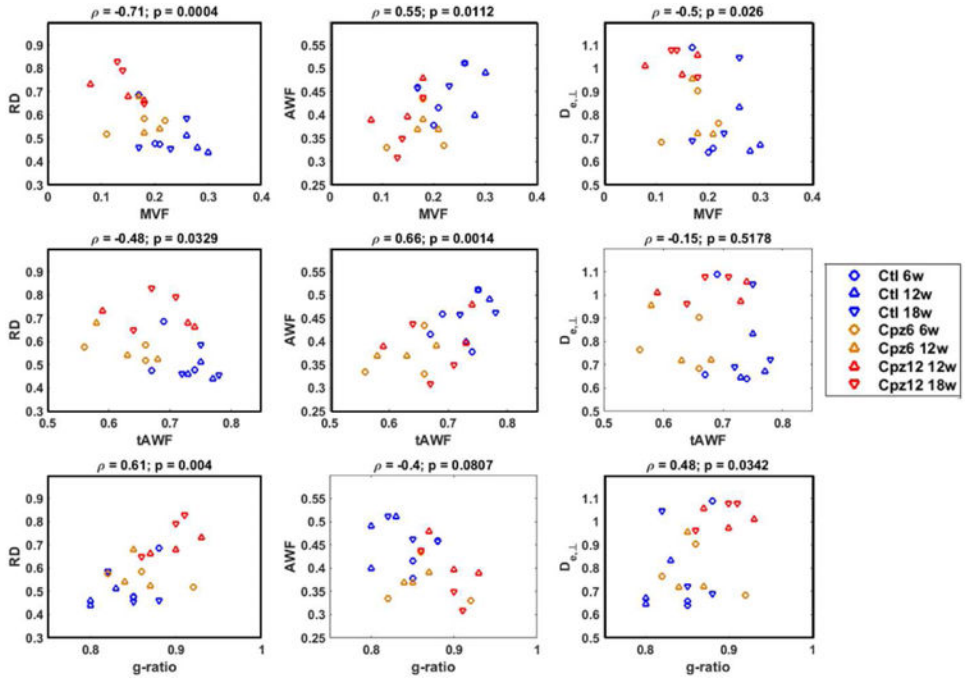

Figure 7.

Representative scatter plots between MR and EM measures. Corresponding correlation coefficients and *p*-values from partial Spearman correlations, controlling for mouse weight at baseline (see Table 2), are provided. The bold frame around the plots indicates a significant correlation. Note the correlations are essentially driven by the differences between the control and the cuprizone groups.

Table 1

P-values, resulting from ANCOVA with Tukey-Kramer multiple comparison correction and mouse weight at baseline as covariate, and Cohen's d, comparing diet arms at each timepoint for a given outcome. No significant differences between the three groups of mice were found at baseline. At 6 weeks, mice in Cpz6 and Cpz12 groups had undergone the same diet (6 weeks of cuprizone); no significant differences between these two groups were found, and they were therefore pooled together for this analysis ("6 weeks" column). Highlighted in green are *p*-values indicative of a significant difference ($p < 0.05$), and in blue the best discriminator between two groups at each timepoint, based on Cohen's d.

	6 weeks		**12 weeks**						**18 weeks**	
	Ctl vs. (Cpz6+Cpzl2)		**Ctl vs. Cpz6**		**Ctl vs. Cpzl2**		**Cpz6 vs. Cpzl2**		**Ctl vs. Cpzl2**	
	***p*-value**	**d**	***p*-value**	**d**	***p*-value**	**d**	***p*-value**	**d**	***p*-value**	**d**
RD	0.0013	1.42	0.3079	0.96	0.0001	2.82	0.0053	1.52	0.2955	0.93
RK	0.0315	-0.88	0.9991	0.02	0.3893	-0.63	0.4122	-0.63	0.085	-1.61
AWF	1.48E-04	-1.68	0.6336	-0.48	0.0108	-1.67	0.098	-1.02	0.2297	-1.08
$D_{e,\perp}$	0.2309	0.49	0.7052	0.45	0.0135	1.58	0.0918	0.99	0.6862	0.32
T_2	8.47E-08	2.77	0.0166	2.69	7.68E-06	3.05	0.021	1.40	0.0545	1.78
MTR	0.008	-1.13	0.5553	-1.12	0.012	-1.49	0.1402	-0.92	0.029	-1.33

Neuroimage. Author manuscript; available in PMC 2017 May 15.

Table 2

Spearman partial correlations (coefficient ρ and p-value) between EM and MR outcomes, covarying for mouse weight at baseline. Significant correlations are highlighted in green ($p < 0.05$).

	MVF		mAWF		tAWF		*g*-ratio	
	ρ	p	ρ	p	ρ	p	ρ	p
RD	-0.71	0.0004	-0.64	0.0023	-0.48	0.0329	0.61	0.0040
RK	0.14	0.5638	0.31	0.1846	0.49	0.0284	-0.04	0.8734
AWF	0.55	0.0112	0.61	0.0046	0.66	0.0014	-0.40	0.0807
$D_{e,\perp}$	-0.50	0.0260	-0.34	0.1379	-0.15	0.5178	0.48	0.0342
T_2	-0.64	0.0024	-0.65	0.0020	-0.42	0.0659	0.52	0.0199
MTR	0.32	0.1821	0.45	0.0522	0.56	0.0117	-0.16	0.5164